Toward Intelligent Wearables: Engineering Self-Powered Triboelectric Nanofibers Sensor for Classification of Risky Ankle Postures

Asma Akter, Gokana Mohana Rani, Md Mehedi Hasan Apu, Yun Suk Huh, Asma Yamani, Abduljabar Q. Alsayoud, Reddicherla Umapathi, Turki N. Baroud**

A. Akter, M.M.H. Apu, Abduljabar Q. Alsayoud, T.N. Baroud

Materials Science and Engineering Department, King Fahd University of Petroleum and Minerals, Dhahran 31261, Saudi Arabia
Email: turkibaroud@kfupm.edu.sa

G.M. Rani

Department of Energy and Materials Engineering, Dongguk University-Seoul, Seoul, 04620, Republic of Korea

Y.S. Huh, R. Umapathi

Department of Biological Sciences and Bioengineering, NanoBio High-Tech Materials Research Center, Inha University, 100 Inha-ro, Michuhol-gu, Incheon 22212, Republic of Korea
Email: umapathi4u@gmail.com

Asma Yamani

Information & Computer Science, King Fahd University of Petroleum and Minerals, Dhahran 31261, Saudi Arabia

T.N. Baroud
Interdisciplinary Research Center for Membranes & Water Security, King Fahd University of Petroleum and Minerals, Dhahran 31261, Saudi Arabia

Table S1. Electrospinning parameters

Parameters	Values
Machine Model	MECC NANON, Japan
Syringe Diameter	16.5 *mm*
Needle gauge	18 *G*
Feed Rate	0.7 *mL/h*
Drum Rotation	200 *rpm*
Spinneret Width	120 *mm*
Spinneret Speed	50 *mm/s*
Spinneret to Drum Distance	15 *cm*
Voltage	24 *KV*
Tip to collector distance	13.5 *cm*

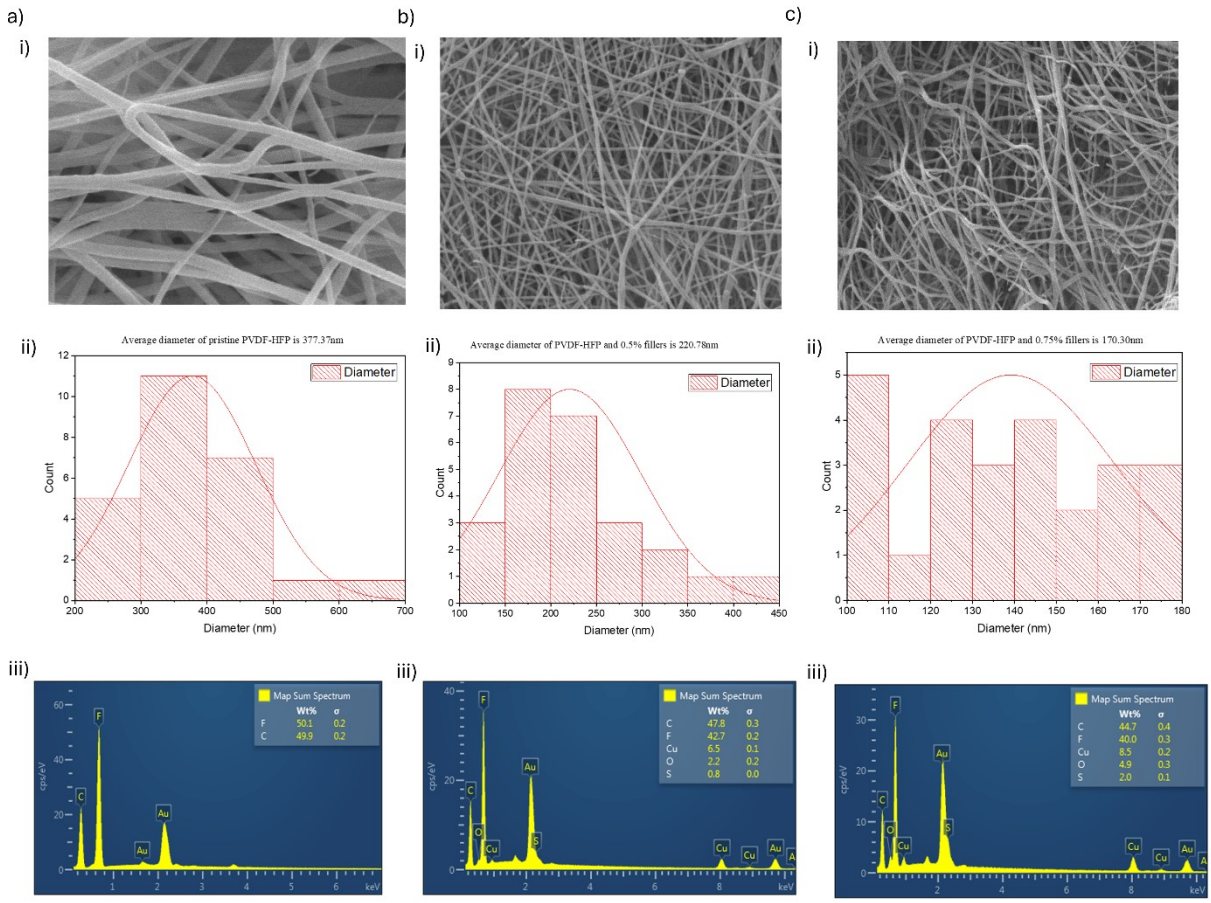

Fig. S1. (a) SEM micrograph of electrospun PVDF-HFP nanofibers (i) Pristine PVDF-HFP (ii) PVDF-HFP with 0.5% fillers and (iii) PVDF-HFP with 1% fillers. (b) EDS spectrum of the nanofibers showing elemental composition with (i) Pristine PVDF-HFP (ii) PVDF-HFP with 0.5% fillers and (iii) PVDF-HFP with 1% fillers.

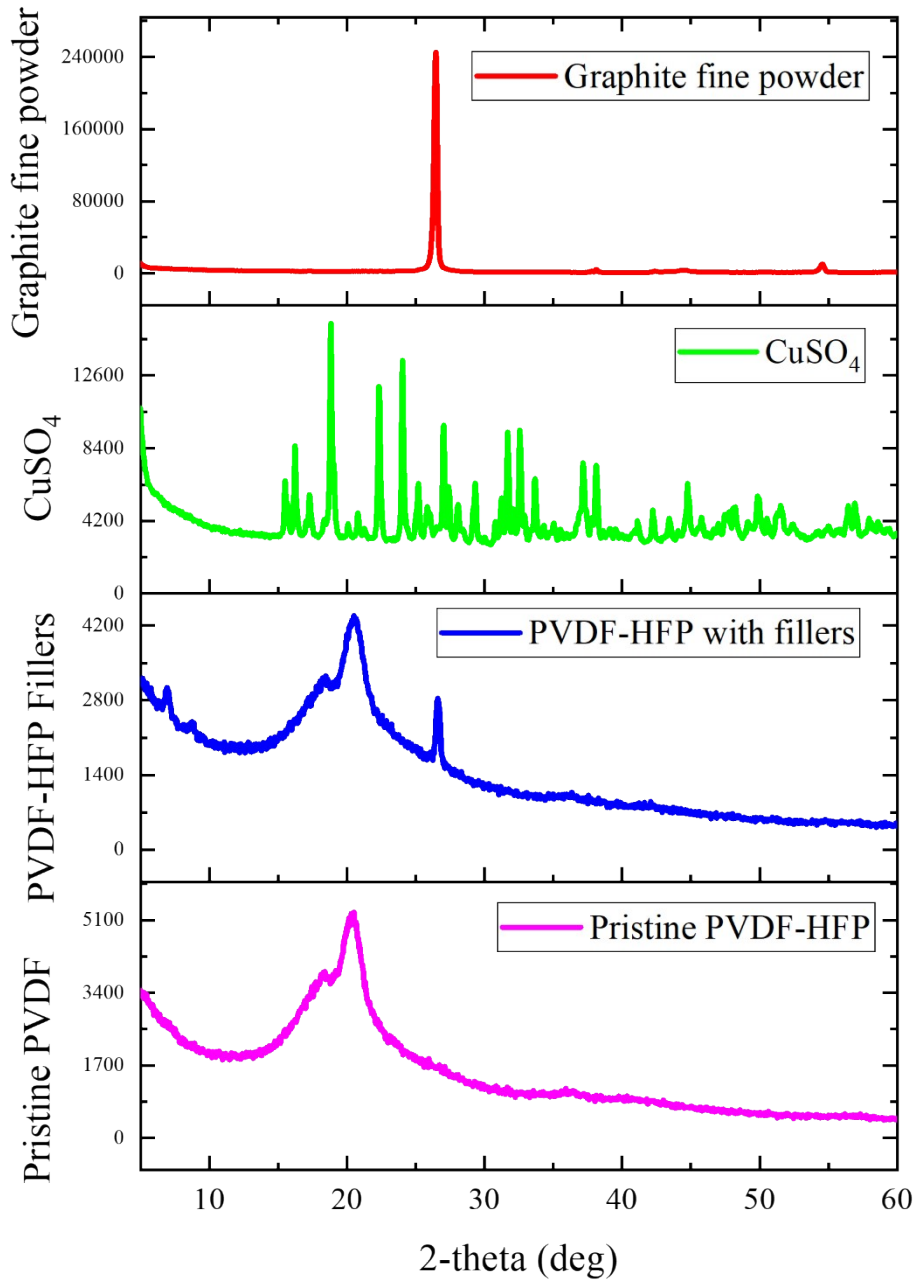

12

13 **Fig. S2.** XRD patterns of pristine PVDF-HFP, PVDF-HFP with fillers, $CuSO_4$, and graphite

14 fine powder.

15

16

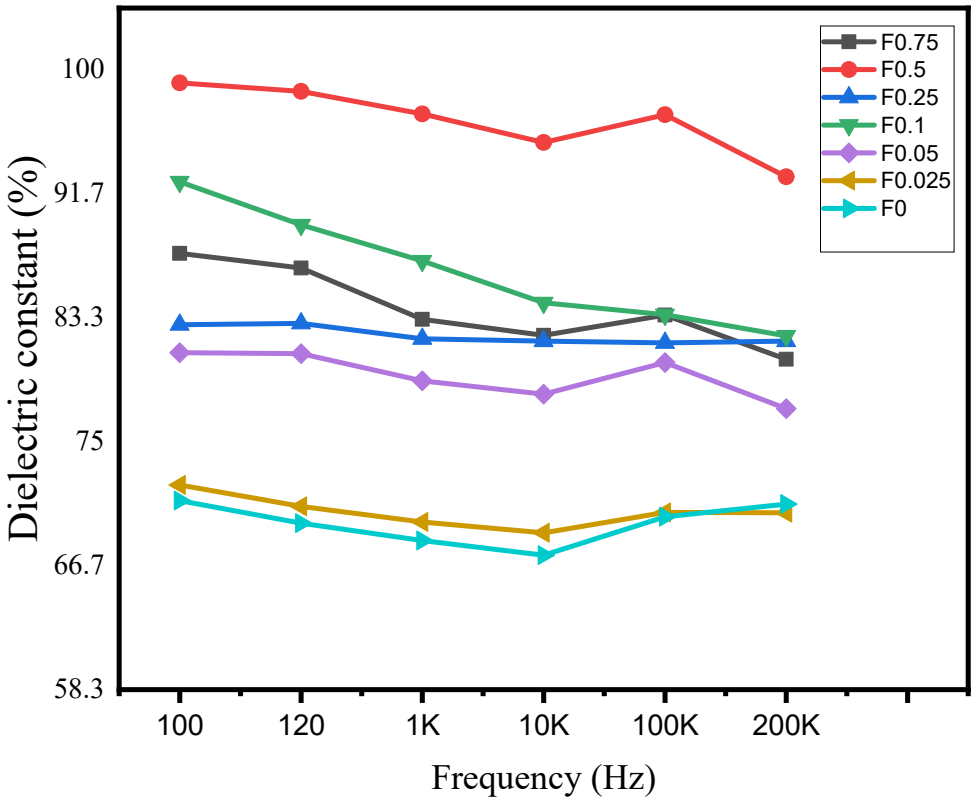

Fig. S3. Dielectric constant of PVDF-HFP/$CuSO_4$/graphite nanofiber mats as a function of frequency for different filler concentrations.

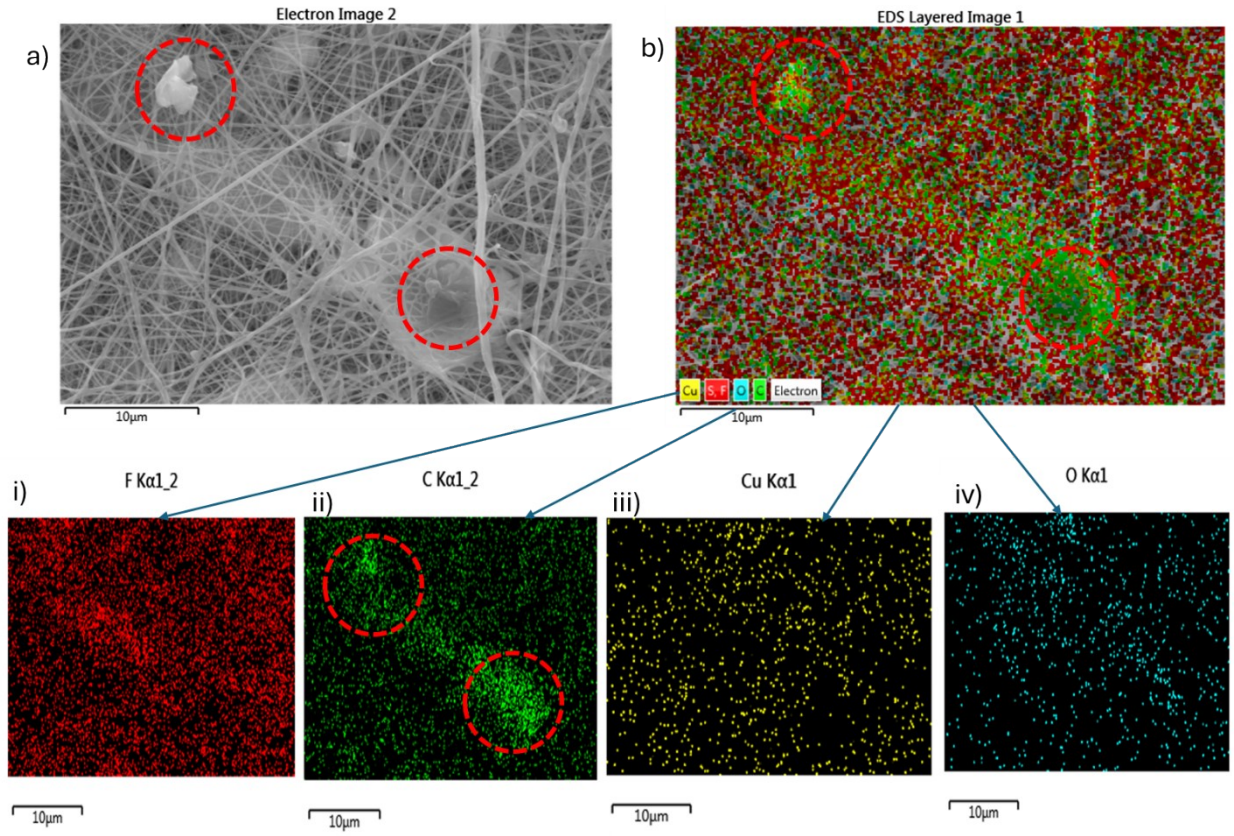

Fig. S4. SEM image analysis of PVDF-HFP with 0.75% fillers.

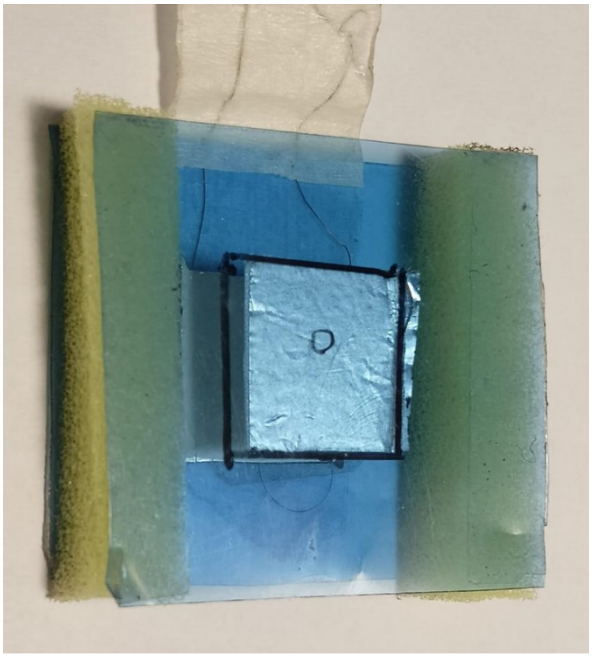

Fig. S5. Photographs of fabricated PHCG-TENG device**.**

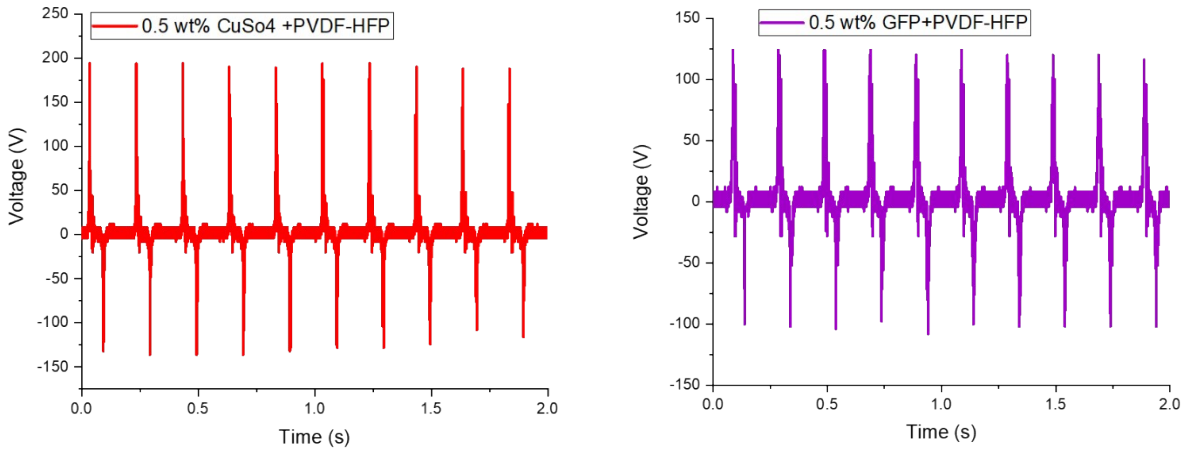

Fig. S6. Triboelectric behaviors of PVDF-HFP nanofiber with 0.5% $CuSO_4$ and 0.5% graphite fine powder.

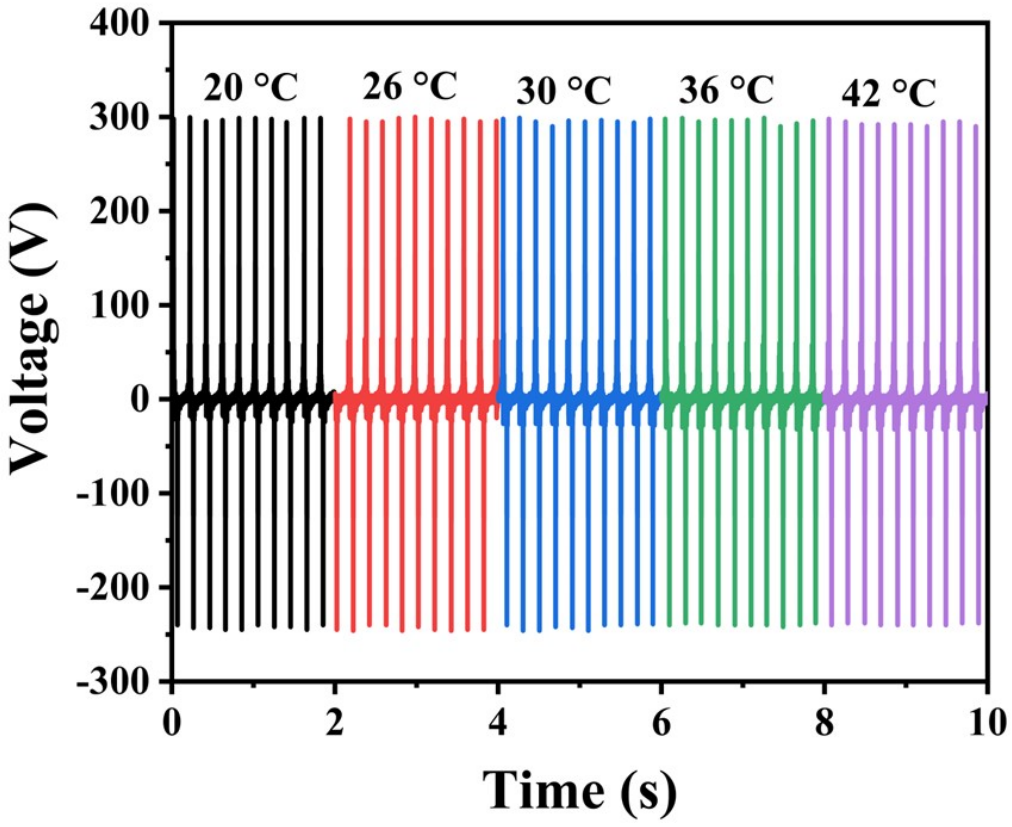

Fig. S7. Triboelectric output voltage of the PHCG-TENG measured under controlled temperature conditions (20 °C, 26 °C, 30 °C, 36 °C, and 42 °C)

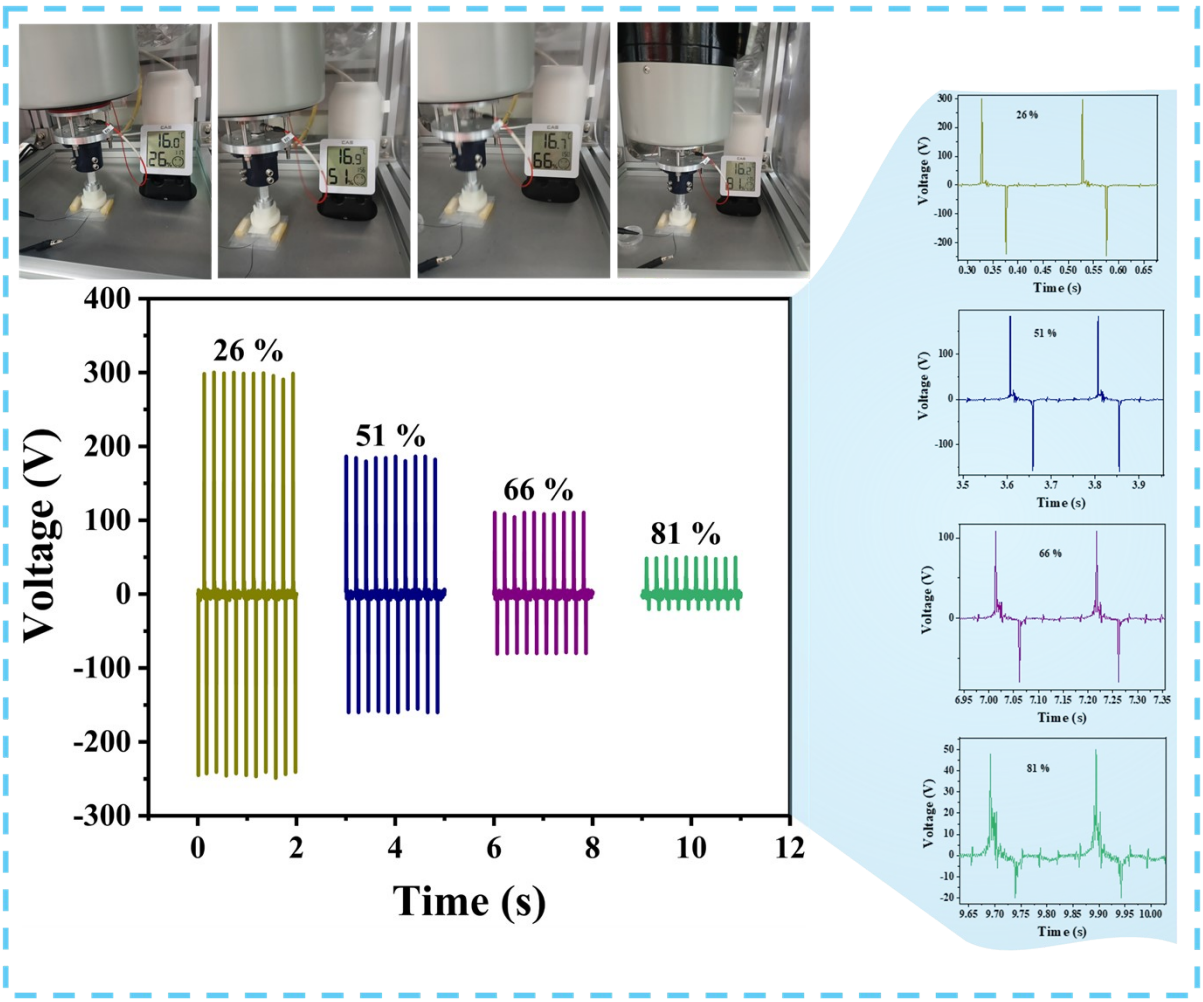

Fig. S8. Triboelectric output voltage of the PHCG-TENG measured under varying relative humidity levels (26%, 51%, 66%, and 81% RH).

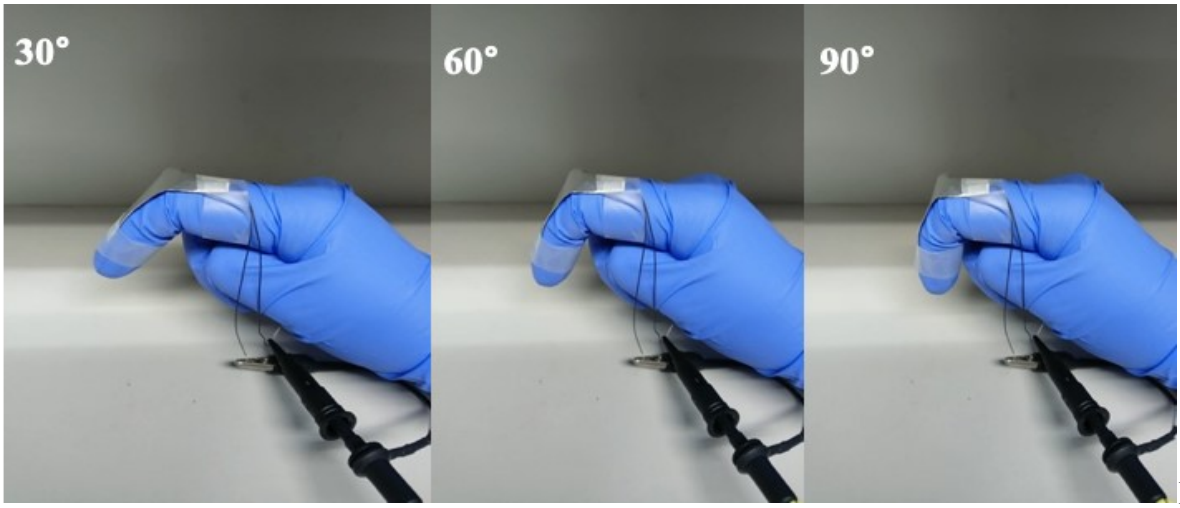

Fig. S9. Photographs showing different finger bending angles used to apply controlled mechanical deformation to the PHCG-TENG for angle-dependent performance evaluation.

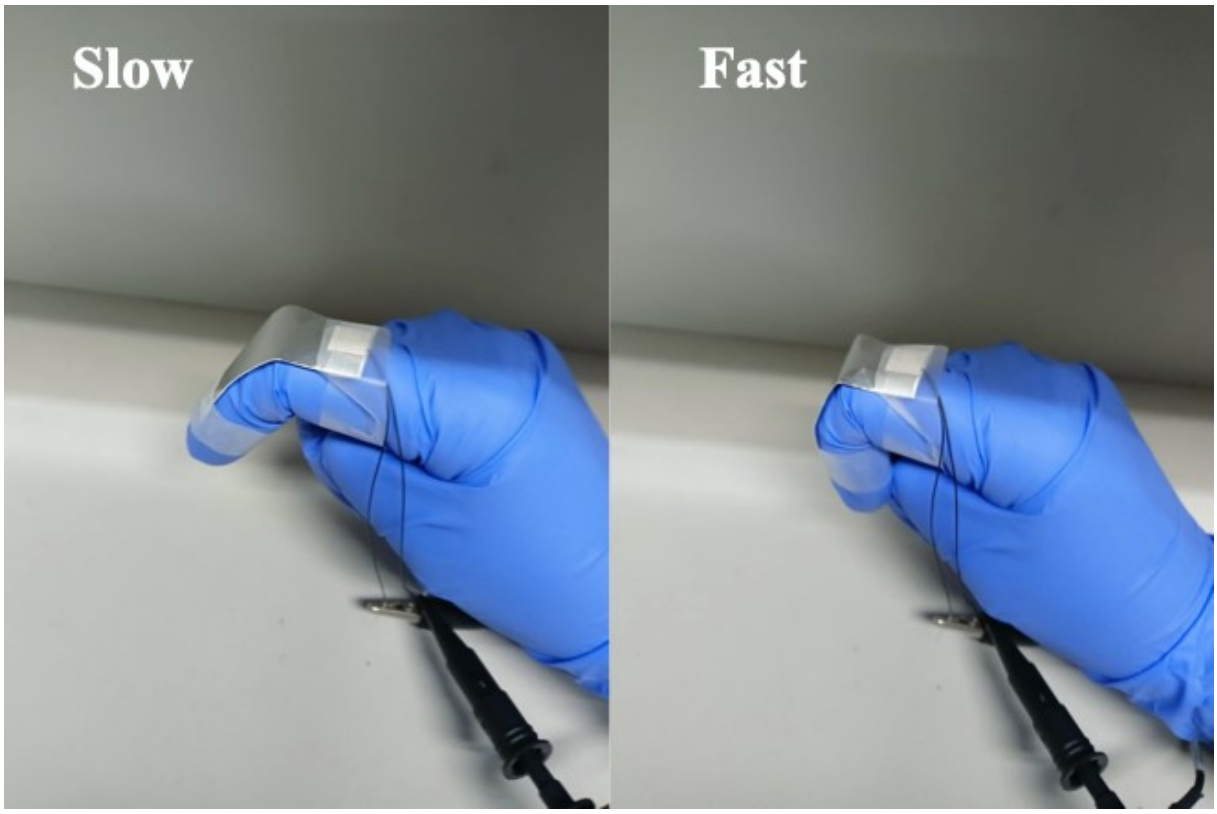

Fig. S10. Experimental demonstration of controlled slow and fast bending motions applied to the PHCG-TENG to investigate deformation rate-dependent electrical output behavior

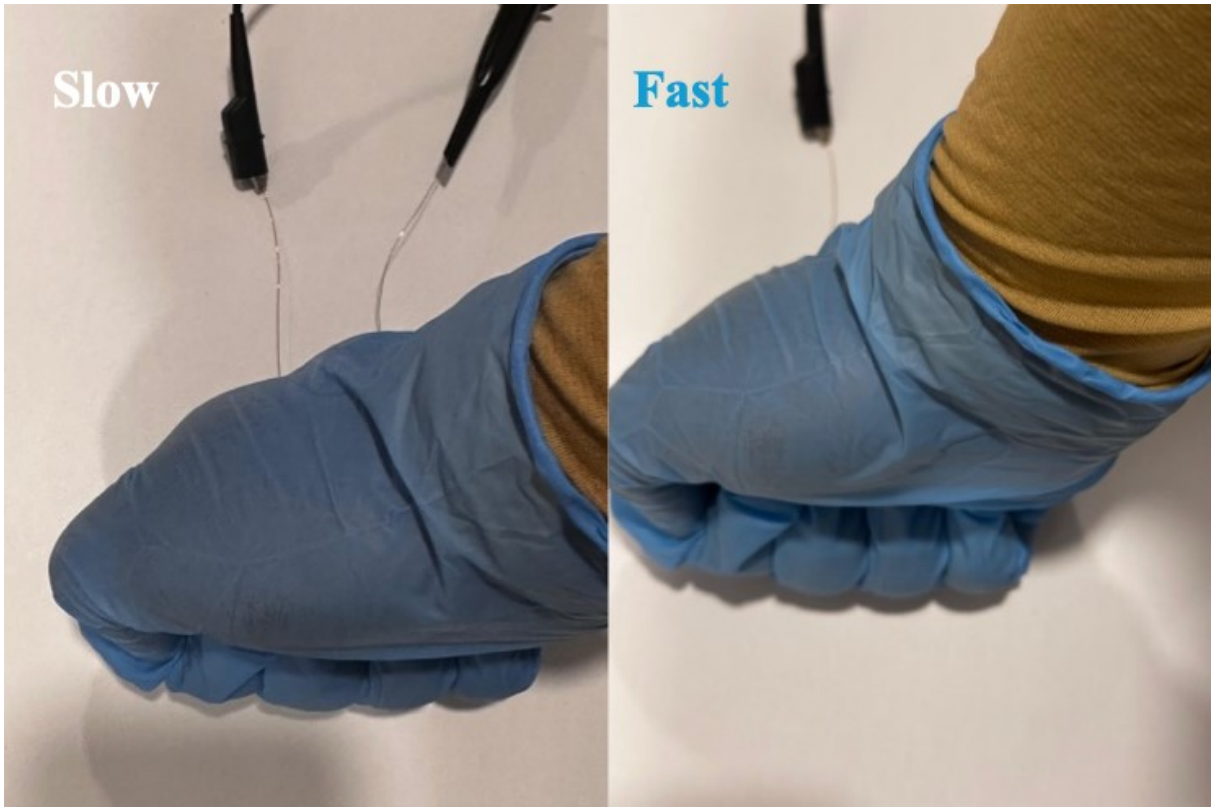

Fig. S11. Experimental demonstration of controlled slow and fast punching actions used to investigate the impact velocity-dependent electrical response of the PHCG-TENG.

Fig. S12. Experimental illustration of 1, 2, and 3 finger contact applied to the PHCG-TENG to investigate the influence of contact area on electrical output performance.

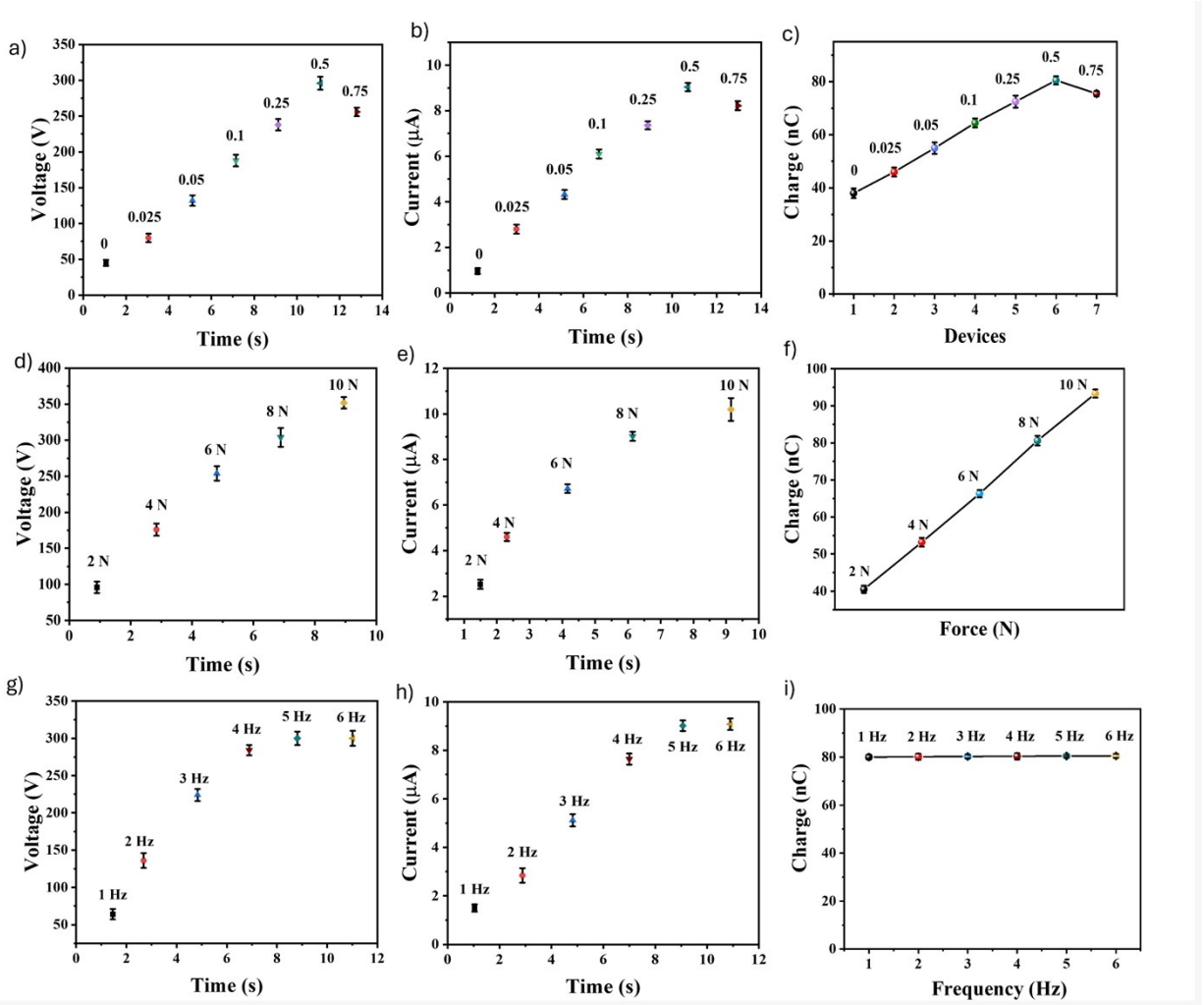

Fig. S13. Electrical output performance of the PHCG TENG with error bars representing measurement variability (a-c) Output voltage, current, and charge for varying filler content of PHCG TENG. The output performance for PHCG TENG under different forces and frequencies (d-f) Voltage, current, and charge response under varying applied forces. (g-i) Voltage, current, and charge response under varying frequencies.

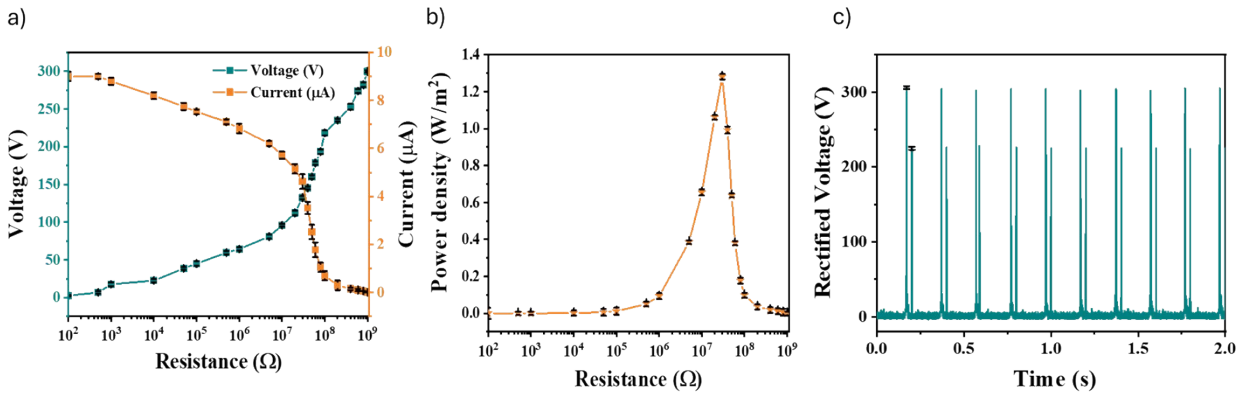

Fig. S14. Electrical performances and practical demonstration of the PHGC TENG with error bars representing measurement variability (a) Voltage and current as a function of load resistance. (b) Power density versus load resistance. (c) Rectified voltage output.

Sensor placement on both ankles | Sensor placement on ankle (Zoomed) | Sensor placement under the Shoe-sole

Fig. S15. Sensor placement for the lateral ankle and insole during testing.

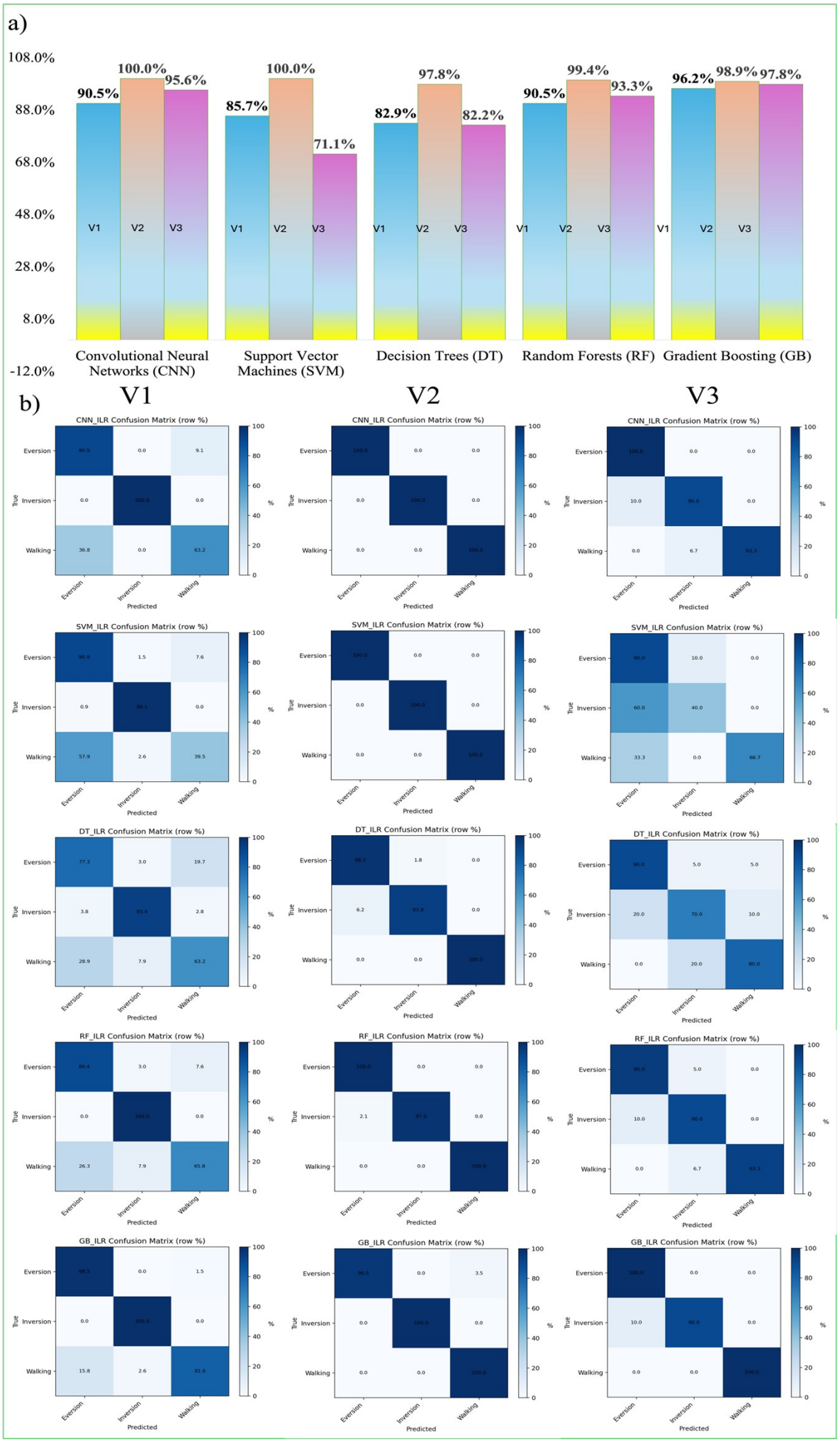
a)
108.0%
88.0%
68.0%
48.0%
28.0%
8.0%
-12.0%
90.5%
100.0%
95.6%
85.7%
100.0%
71.1%
82.9%
97.8%
82.2%
90.5%
99.4%
93.3%
96.2%
98.9%
97.8%
V1
V2
V3
Convolutional Neural Networks (CNN)
Support Vector Machines (SVM)
Decision Trees (DT)
Random Forests (RF)
Gradient Boosting (GB)
b)
V1
V2
V3
CNN_ILR Confusion Matrix (row %)
SVM_ILR Confusion Matrix (row %)
DT_ILR Confusion Matrix (row %)
RF_ILR Confusion Matrix (row %)
GB_ILR Confusion Matrix (row %)
Eversion
Inversion
Walking
True
Predicted
%

Fig. S16. Classification performance of multiple machine learning algorithms for detecting ankle motion patterns from PVDF-HFP/$CuSO_4$/graphite TENG sensor signals. (a) Classification accuracy for convolutional neural networks, support vector machines, decision trees, random forests, and gradient boosting using different datasets (V1 – V3). (b) Corresponding confusion matrices for each motion class (eversion, inversion, walking) across selected datasets.

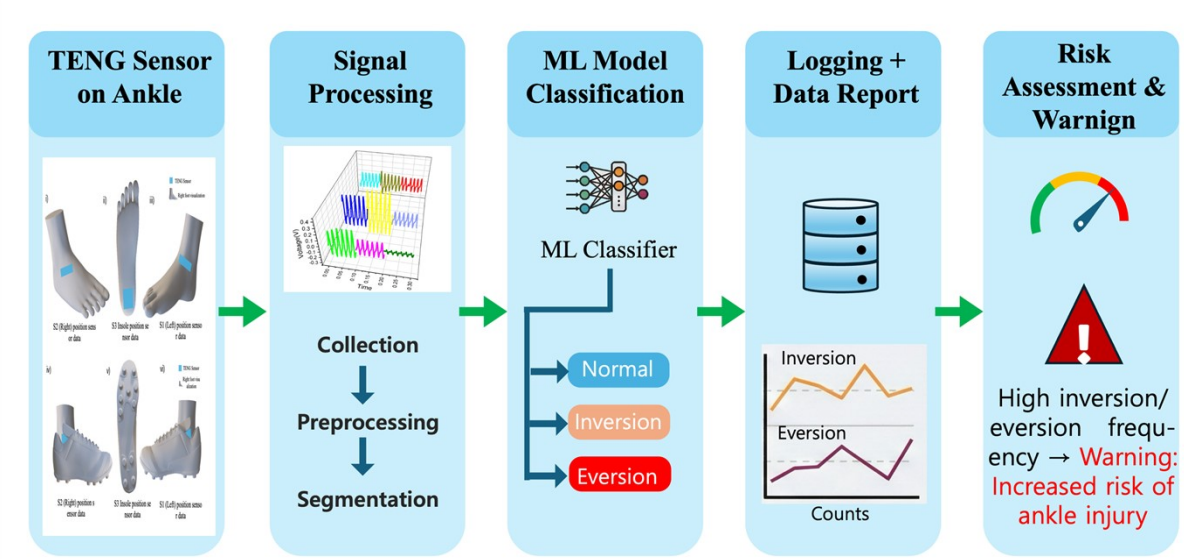

Fig. S17. Schematic diagram of the proposed real-time processing and system integration framework for early ankle injury prediction (future work).

Table S2. Accuracy (%) of different machine learning models (CNN, SVM, DT, RF, GB) across three volunteers (V1–V3) for a dataset size of 300.

	Accuracy over volunteer(dataset size: 300)		
Model Name	**V1**	**V2**	**V3**
Convolutional Neural Networks (CNN)	77.8%	100.0%	95.60%
Support Vector Machines (SVM)	75.6%	95.6%	71.10%
Decision Trees (DT)	73.3%	95.6%	82.20%
Random Forests (RF)	82.2%	95.6%	93.30%
Gradient Boosting (GB)	82.2%	97.8%	97.80%

91